



University
of Glasgow

Robb, P.D., Finnie, M., and Craven, A. (2012) *Modelling of AlAs/GaAs interfacial structures using high-angle annular dark field (HAADF) image simulations.* Ultramicroscopy, 118. pp. 53-60. ISSN 0304-3991

<http://eprints.gla.ac.uk/66658/>

Deposited on: 29 June 2012

Modelling of AlAs/GaAs interfacial structures using high angle annular dark field (HAADF) image simulations

Paul D. Robb^{1,2*}, Michael Finnie¹, Alan J. Craven^{1,2}

¹SUPA School of Physics & Astronomy, University of Glasgow, G12 8QQ, UK

²SuperSTEM Laboratory, Daresbury Laboratory, WA4 4AD, UK

**Correspondence:* Room 402
Department of Physics and Astronomy
University of Glasgow
Glasgow G12 8QQ
paul_robb@live.co.uk

Abstract

High angle annular dark field (HAADF) image simulations were performed on a series of AlAs/GaAs interfacial models using the frozen-phonon multislice method. Three general types of model were considered- perfect, vicinal/sawtooth and diffusion. These were chosen to demonstrate how HAADF image measurements are influenced by different interfacial structures in the technologically important III-V semiconductor system. For each model, interfacial sharpness was calculated as a function of depth and compared to aberration-corrected HAADF experiments of two types of AlAs/GaAs interfaces. The results show that the sharpness measured from HAADF imaging changes in a complicated manner with thickness for complex interfacial structures. For vicinal structures, it was revealed that the type of material that the probe projects through first of all has a significant effect on the measured sharpness. An increase in the vicinal angle was also shown to generate a wider interface in the random step model. The Moison diffusion model produced an increase in the measured sharpness with depth which closely matched the experimental results of the AlAs-on-GaAs interface. In contrast, the measured sharpness decreased as a function of depth in the linear diffusion model. Only in the case of the perfect model was it possible to ascertain the underlying structure directly from HAADF image analysis.

Keywords: HAADF imaging; multislice simulations; interfaces; semiconductors

1. Introduction

The ability to control the growth of semiconductor layers to the width of a few atomic layers is becoming increasingly important for the development of new high-speed semiconductor devices [1-3]. Growth techniques, such as molecular beam epitaxy (MBE), are often employed to deposit individual atomic layers to construct complex heterostructures [4]. High-angle annular dark field (HAADF) imaging in scanning transmission electron microscopy (STEM) is regularly used to characterise these materials [5-6]. With the improved spatial resolution offered by aberration-corrected instruments, it is now standard practice to study the quality of interfacial structures at the atomic scale [7-8].

The atom column intensities in a HAADF image are sensitive to the average atomic number (Z) [9-11]. In a simple model of image contrast, a column signal is generated by the high-angle scattering from the channelled region of an atomic column [12-14]. In comparison, it is assumed that the underlying background signal is generated from the average scattering from the material volume that is sampled by the de-channelled probe and therefore provides non-local information [12]. With consideration to this model, the background signal is often removed and analysis is only performed on the remaining column signals. Although this is a qualitative model, it does allow a quantitative comparison to be made between experiment and simulation once the background signal is removed from both. This circumvents the traditional contrast problem of the simulations and it is the approach taken in this paper. In order to take advantage of the high-spatial resolution information of the column signals, a method of analysis was developed for the III-V semiconductor system oriented in the $\langle 110 \rangle$ direction [15]. In this approach, interfacial sharpness was measured by examining the change in the ratio of the Group III and Group V column signals (without the background contribution) across each atomic row to give an average interfacial width.

An improved analytical technique was also employed to investigate the sharpness of two types of AlAs/GaAs interface as a function of specimen thickness [16]. In the case of the GaAs-on-AlAs interface (i.e. GaAs grown on top of AlAs) it was found that the average interface width showed no variation with thickness. In contrast, it was shown that the opposite configuration of AlAs grown on top of GaAs (termed an AlAs-on-GaAs interface) revealed an interface width that was strongly dependent on the specimen thickness. Hence, it is not always sufficient to assess the quality of an interfacial structure from a single image

especially in cases where the composition changes in three dimensions. It is also unclear how, for example, different levels of elemental diffusion or stepping in each dimension would translate into image contrast and the final assessment of the interface. Thus, important details about the structure and arrangement of interfacial structures cannot be ascertained directly from the experimental results and image simulations are required for interpretation.

HAADF image simulations must include both elastic and thermal diffuse scattering for a quantitative analysis [17-18]. The frozen-phonon multislice method incorporates both types of scattering and has been used extensively to make quantitative comparisons with experimental HAADF images for many types of material [19-20]. Moreover, it has been shown that if images are collected on an absolute intensity scale and the simulations include a finite effective source size an excellent agreement between simulation and experiment is obtained and there is no need for intensity scaling [21-24].

In this paper, the frozen-phonon multislice technique is used to simulate a series of AlAs/GaAs models in order to examine how complex interfacial structures can affect HAADF imaging results. The AlAs/GaAs system was chosen for study to allow a comparison to be made with the previously reported experimental results and also due to its application in high-mobility semiconductor devices [16,25-27]. The models can be grouped into the three basic types of perfect, vicinal/sawtooth and diffusion. The range of models considered permits different interfacial characteristics to be investigated and whether the differences can be detected and distinguished using HAADF imaging. Each model is simulated at every atomic slice up to a thickness of 100nm and the variation in the measured interfacial width is displayed alongside the previous experimental results. This approach allows likely candidate models of interfacial structure to be selected for the experimental results and therefore an improved assessment of interface quality to be made.

2. Method

2.1 Experimental

The 100kV SuperSTEM 1 instrument was used to obtain all of the experimental data [28-29]. This aberration-corrected microscope corrects aberrations up to 5th-order. The cold FEG of the instrument has a gun brightness of about $10^9 \text{Acm}^{-2}\text{Sr}^{-1}$ and an energy spread of 0.3eV. A Gatan-ENFINA spectrometer with an energy resolution $\sim 0.35\text{eV}$ was used to collect electron

energy loss spectroscopy (EELS) data. All HAADF images were acquired using a probe semi-convergence angle of 24mrad, a pixel dwell time of 19 μ sec, a pixel size of 0.0146nm and were composed of 1024 \times 1024 pixels. The inner and outer angles of the HAADF detector were 70mrad and 210mrad, respectively. The image intensity black level was set so that a few image counts (~5-10) were recorded above the noise in the absence of any specimen material. Image counts are typically of the order of several thousand in the presence of a specimen. Images were discarded that did not show Fourier reflections up to a spatial resolution of 1 \AA and that were not from a uniform and flat specimen area. In order to measure the specimen thickness of a particular image, the probe was scanned rapidly across the entire image area and 50 low loss EELS spectra were averaged together. The absolute specimen thickness was then calculated using the method described by Egerton [30].

AlAs/GaAs interfaces, bulk AlAs and bulk GaAs were grown epitaxially on a GaAs wafer along the [001] crystal direction by MBE. The conventional cross-section technique was employed to prepare the specimen which was finished with a low energy ion mill at 400eV and at an angle of 6 $^\circ$ using a Technoorg GentleMill [31]. All of the experimental data was acquired with the specimen oriented along the [110] direction. This crystal projection forms the distinctive dumbbell configuration of zinc-blende materials in which a dumbbell is constructed from a column of Group III atoms (Al or Ga) and a column of Group V (As) atoms. Distances are given in terms of monolayers (ML) where 1ML is equal to distance between successive dumbbells along the [001] direction. The Z numbers of Al, Ga and As are 13, 31 and 33, respectively.

HAADF images of AlAs-on-GaAs and GaAs-on-AlAs interfaces were taken over a range of specimen thicknesses. The images were analysed and plots of the interfacial width as a function of specimen thickness were produced for both types of interface. The method of analysis is described in detail in [16]. In brief, each interface image was firstly converted into a map of the dumbbell column ratio which is defined as $(I_{\text{III}} - I_{\text{BD}}) / (I_{\text{V}} - I_{\text{BD}})$. I_{III} and I_{V} are the total HAADF signals at the Group III and Group V columns of a particular dumbbell, respectively [15]. I_{BD} is the background signal for each column in the dumbbell. Line profiles of the column ratio were then taken across each atomic row of the interface (i.e. always along the [001] growth direction) and an analytical function was fitted to each profile. The 5% to 95% width of the function was used as a measure of the interfacial width in each case. The interfacial width defines the extent of the transition region between the two bulk materials. In

addition, the inflection point of the fitted function was used to define the apparent position of the interface. The average interface width was then calculated and the process was repeated for each image in the thickness series. The plots of the interfacial width presented in this paper were replicated from [16].

2.2 Simulation

HAADF STEM calculations were performed using frozen-phonon multislice code adapted from Kirkland [32]. An effective source size was not included and the analysis implemented the background-removal technique in order to compare the column signals (via the column ratio) generated by the simulations with those from the experimental results. The exclusion of an effective source size will likely have a small effect on the simulated column ratio values but not on the interface widths or positions which are the important attributes under scrutiny in this paper. Simulated parameters were chosen to match the SuperSTEM 1 probe and the experimental conditions. The simulated probe was formed using an accelerating voltage of 100kV, a convergence semi-angle of 24mrad and aberration coefficients up to and including $C_{5,6}$ (6-fold astigmatism of C_5). This generated a $\sim 1\text{\AA}$ probe at FWHM (full width at half maximum) with $\sim 57\%$ of the total probe intensity contained within the central peak. The HAADF detector angles also matched those of SuperSTEM 1. To simulate the effect of thermal vibrations on the HAADF signal, the Einstein model for phonon vibrations was implemented at a temperature of 300K [32]. 100 phonon configurations were chosen to give a smaller error in the simulated column ratio values than that measured experimentally ($\sim 1-2\%$). The Debye-Waller factors and atomic displacements for the atoms in AlAs and GaAs were taken from [33]. Other sources of atomic displacement may exist for diffused and stepped interfaces such as strain and structural relaxation effects. These would also likely alter the HAADF signal in a manner similar to the Debye-Waller factor. However, due to difficulty in modelling these effects, they were not included in the simulations and their exclusion may introduce a small error in the diffused and stepped models. The calculations were performed using the ScotGRID computer system based at the University of Glasgow [34].

The starting point for each interfacial model was a supercell made from a perfect AlAs/GaAs interface with the probe directed along [110]. The supercell was composed of 8×16 [110]-unit cells of AlAs joined to 8×16 [110]-unit cells of GaAs without any strain. Fig. 1 shows a

schematic of the supercell for reference. The supercell was $90.5\text{\AA}\times 64.0\text{\AA}$ (i.e. 32×32 dumbbells) in size, had a slice thickness of 2.0\AA and was constructed from 2048×2048 pixels for adequate sampling in real and reciprocal space [32]. A custom script allowed the composition of an 8 dumbbell wide strip across the interface boundary to be varied in three dimensions to generate a particular model structure. Each model was constructed up to a thickness of 100nm (500 slices).

Calculations were performed across each interface (at every slice thickness) for a 16 dumbbell wide line trace along the central interleaved dumbbell row of the supercell (see Fig. 1). In order to match the experimental column ratio analysis, discrete probe positions were chosen to be simulated along the line. This was also necessary to reduce the prohibitive CPU time required to simulate a full STEM profile for each model at every thickness [35]. For each of the 16 dumbbells, I_{III} , I_V and I_{BD} were simulated (the inset of Fig. 1 shows these positions for a particular dumbbell) and the column ratio calculated. The method of analysis previously outlined for the experimental data was then applied to the simulated column ratio profiles [16]. In this way, the interfacial width as a function of specimen thickness was determined for each model up to 100nm. It should be noted that at thicknesses greater than 100nm, the scattered real space intensity within the crystal approaches the sides of the supercell for probe positions at either end of the simulated line trace. However, since dumbbells 1-4 and 13-16 along the simulated line trace are always either bulk AlAs or bulk GaAs it was verified that there was no change in the HAADF signals or column ratios of these end dumbbells.

In order to test the validity of the simulated conditions, calculations of the column ratio for bulk AlAs and bulk GaAs were also performed and compared to experimental values. Fig. 2(a) reveals that there is a good correspondence between the simulated and experimental column ratios for both materials as a function of thickness. This suggests that the exclusion of an effective source size and other possible sources of error in the simulations are not too significant in this case. Each experimental data point has a standard error of 1-2% and was obtained from averaging over 600 dumbbells. The increase in the AlAs column ratio is a result of the weakly scattering Al columns retaining a portion of the probe intensity to large crystal depths in contrast to the Ga columns. The difference in the channelling depths of Al, Ga and As (from GaAs) columns can be seen in Fig. 2(b) where the simulated real space intensity contained within a 0.2\AA radius of the atom cores is shown as a function of thickness.

Whereas the Ga and As columns have a channelling depth of about ~20nm, Al columns still retain some probe intensity at 100nm. In addition, all columns focus the probe intensity to give a maximum value at a depth of ~3.5nm.

3. Results and Discussion

3.1 Perfect Model

The perfect model was the first to be simulated and consisted of an ideal interface between AlAs and GaAs. The purpose of such a simple structure was to give a basic understanding of the simulated methods and to provide a benchmark for the other more complicated models. Fig. 3 presents a side view schematic of the perfect model down to a thickness of 100nm and along the 16 dumbbell wide simulation line. Fig. 3 shows that the perceived interface position remains at the boundary throughout the depth of the model. Fig. 4 is a plot of the interface width, measured in monolayers, versus specimen thickness and demonstrates that the sharpness of the perfect model remains constant. In this case, it would be a simple matter to interpret HAADF imaging results. The reason that the perfectly abrupt interface has a non-zero interface width (~0.9ML) is the result of fitting an analytical function to discrete data points and using the 5% to 95% limits as a measure of the interface width. It is apparent that the perfect model does not match the experimental results indicating that the two types of interfaces do have an underlying interfacial structure. Furthermore, the perfect model confirms that the experimental behaviour is not simply the result of beam spreading across an ideal interface.

3.2 Vicinal/Sawtooth Models

During the MBE growth process, layers are deposited on a [001] oriented GaAs substrate which is polished to a tolerance of $\pm 1/2^\circ$ [1]. This can lead to a vicinal interface in which the layers are inclined at an angle θ with respect to the incident probe [26]. A vicinal structure is a specific case of a more general interface form termed a sawtooth in which the angle of inclination repeatedly changes direction through the thickness of the material. Fig. 5 shows a schematic of a sawtooth model which has a characteristic step length (L) of 7.2nm (36 slices) and a repeat length (R) of ~108nm which is slightly greater than the maximum simulation depth. This particular step length was chosen to match previous observations of the average step length in the AlAs/GaAs system [25]. For the top half of the repeat, the model behaves

like a vicinal structure with $\theta=2.2^\circ$ which is larger than the usual polishing tolerance. Nonetheless, simulation of this model is instructive for establishing the likely behaviour of vicinal interfaces. The two interfaces illustrated in the schematic were simulated separately using an independent supercell to set up each standalone interface. Due to the geometry of the model, the probe either projects through a top section of AlAs (AlAs-projection) or GaAs (GaAs-projection) at the interfaces (see Fig. 5).

The apparent interface position of the AlAs-projection follows the inclination of the stepping to a thickness of $\sim 57\text{nm}$. This behaviour is due to the introduction of heavier Ga atoms to the bottom of the 100% Al columns which increases the high angle scattering to produce a column signal similar in strength to a bulk Ga column in the neighbouring GaAs. Hence, the dumbbells across the stepped interface appear to become part of the GaAs region as the thickness is increased and the interface position shifts towards the bulk AlAs region. This means that the apparent size of the GaAs layer (given by the distance between the interface positions) also expands with thickness as can be seen in Fig. 5. Thus, the measurement of layer sizes using HAADF imaging is not a straightforward matter for vicinal/sawtooth structures. At a depth of $\sim 57\text{nm}$, the maximum lateral protrusion of the repeat is reached and the structure then acts in a similar manner to a flat interface positioned between dumbbells 27-28. In the GaAs-projection case, the initial overhang of GaAs causes the columns to generate a column signal similar to a bulk Ga column at much lower depths and the interface position only marginally shifts towards the GaAs layer. This demonstrates that compositional changes at large depths cannot be probed and detected in a standard HAADF image if a significant amount of a high Z material is projected through first of all. This is related to the relatively short channelling depths of high Z atomic columns such as Ga.

The change in the interface width for the two projection cases can be seen in Fig. 4. They behave exactly like the perfect interface up to the depth at which the first step is introduced (7.2nm) as expected. For the AlAs-projection case, the interface width then rises to a value of $\sim 4\text{ML}$ at a depth of $\sim 28\text{nm}$ (the depth at which 3 steps are present) which is a fair reflection of the underlying stepped structure. At greater thicknesses, the interfacial dumbbells become GaAs-like and the interfacial width decreases. On the other hand, the interfacial width for the GaAs-projection case rises to a value of $\sim 2.3\text{ML}$ at a depth of $\sim 28\text{nm}$ and then gently rises up to a value of $\sim 3\text{ML}$ at a depth of $\sim 80\text{nm}$. It is clear that the two simulated interfaces do not produce the variation in the width observed for the AlAs-on-GaAs experimental data but both

could be a potential candidate for GaAs-on-AIAs. However, since the vicinal angle of the model is larger than that expected of the MBE process, it is unlikely that the experimental interfaces have such a structure.

A second sawtooth model was considered with a very short step length of 1.2nm (6 slices) and a repeat length of 19.2nm which is similar to the Ga channelling depth. Fig. 6 displays the schematic for this model. In a similar fashion to the previous sawtooth model, the apparent interface position of the AIAs-projection generally follows the inclination in the top half of the first repeat and shifts towards the bulk AIAs region as Ga is added into the columns. After a depth of ~12nm, the interface position stops moving towards the AIAs region as not enough Ga is present in dumbbells 24-27 to generate a bulk Ga column signal. Correspondingly, the interface width at this depth reaches a maximum value of ~5ML as shown in Fig. 4. At greater depths, the interface width tends towards a value of ~3-4ML as dumbbells 25-27 always form the transition region between AIAs and GaAs. In this thickness range the AIAs-projection shows a similar behaviour to the GaAs-on-AIAs experimental data.

For the GaAs-projection case, the small entry steps of GaAs near the top surface are not enough to generate a bulk Ga column signal from dumbbells 6-11. Hence, the interface position shifts towards the GaAs layer as the interfacial region widens at depth. This is unlike the first sawtooth model in which the longer GaAs-projected steps generated bulk Ga column signals quite readily. At a thickness of ~20-40nm, dumbbells 5-11 form the transition region and the interface width reaches a maximum value of ~8ML which is much wider than the AIAs-projection case. Dumbbell 12 acts like bulk GaAs at all depths of the model. As the thickness increases, dumbbells 5-8 appear to become more AIAs-like and the interface position shifts towards the GaAs layer and the interface width shrinks accordingly. Fig. 4 also illustrates that the GaAs-projection plot does not match any of the experimental data sets.

The behaviour of dumbbells 5-8 can be explained by examining the effect of the periodic introduction of Ga on the HAADF column signals. Fig. 7 gives the (background-removed) HAADF signal of the Group III column of dumbbell 7 with the position of the GaAs steps overlaid. Also shown are the equivalent plots of bulk Al and Ga columns. As more Ga is added into the column of dumbbell 7, dynamical re-scattering effects start to dominate (in the same way as with the bulk Ga column) and the HAADF column signal drops off. As the thickness increases, the column signal from dumbbell 7 approaches the rising Al column

signal and it eventually becomes indistinguishable from a bulk Al column. Above ~80nm, the dumbbell 7 column signal then drops below that of bulk Al despite the possessing a larger average Z number.

Both sawtooth models demonstrate that variations in step and repeat lengths can be differentiated using HAADF imaging although simulations are required to estimate the likely underlying structure. It is also apparent that significant differences in the measured interfacial quality can arise if low or high Z material is projected through first of all. In addition, although three of the sawtooth interfaces did show some agreement with the GaAs-on-AlAs experimental data, it is unlikely that structures with such regular and consistent stepping are formed by MBE. For instance, it has been reported that under certain growth conditions a range of step lengths can exist in the AlAs/GaAs system [25].

To simulate a more realistic vicinal structure, models were created in which random stepping was overlaid onto vicinal interfaces. Vicinal angles of $\theta=0.2^\circ$, 0.3° and 0.6° were considered. Individual step lengths were chosen from a Gaussian distribution with mean value of 7.2nm and were randomly positioned along each interface. To ensure that the results were not sensitive to one particular random arrangement, 10 independent configurations for each interface were simulated separately and then averaged together during analysis. This is equivalent to averaging over many different dumbbell rows in the experimental analysis. To limit the required computational time, only the AlAs-projection case was simulated.

The schematic of the random step 0.6° interface is shown in Fig. 8(a). As was the case for the previous sawtooth models, the interface position shifts towards the AlAs region as the column signals become similar to bulk Ga columns with increasing thickness. The shift in the interface position also continues up to the maximum simulation depth as the projection through low Z AlAs allows the compositional changes of the deeper steps to be detected. Fig. 8(b) reveals the variation in the interface width for the 0.2° , 0.3° and 0.6° models. It can be seen that the random step models produce plots of the interface width that better resemble the behaviour of the experimental AlAs-on-GaAs interface in contrast to the previous models. The vicinal angle also has an effect on the interface width with the 0.6° model generating the largest values due to the presence of more steps in the structure compared to the lower angle models. Hence, differences in the degree of vicinality of interfacial structures can be detected and explored using HAADF imaging. Nevertheless, the 0.6° model still does not generate

interface widths that are as large as the AlAs-on-GaAs experimental plot. If the vicinal angle is increased it is likely that a suitable match would be produced but the vicinal angle would be larger than the expected tolerance of the MBE process.

3.3 Diffusion Models

The presence of a chemical potential gradient during MBE growth can lead to the formation of a diffused interface in which the Group III atoms intermix over a certain range [1]. The schematic of a simple linear diffusion model is given in Fig. 9(a). The change in concentration of Al and Ga across the interface is provided in Fig. 9(b). A random number generator was used to populate each interfacial dumbbell with the required concentration of Al and Ga. The calculation results from 10 independent configurations were averaged together in a similar fashion to the random step models.

Fig. 10 demonstrates that the interface width does not match any of the experimental data sets. For instance, the modelled interface is very wide (~8ML) for very thin crystals and progressively narrows as the thickness is increased. This is due to the high Ga content columns of dumbbells 5-7 generating column signals comparable to bulk Ga columns as the thickness is increased. This effect is also reflected in the shift of the interface position towards the AlAs region as shown in Fig. 9(a). The simple linear diffusion model highlights that columns that contain up to 33% Al (i.e. dumbbells 5-7) will be indistinguishable from bulk Ga columns for HAADF experiments conducted at typical specimen thicknesses (~30nm). Hence, it would be difficult to properly characterise this type of interface using a single HAADF image.

A more realistic model of diffusion in the AlAs/GaAs system was developed by Moison et al in which the AlAs-on-GaAs interface exhibited a gradual compositional change over 8ML and the GaAs-on-AlAs interface displayed a more abrupt change over 4ML [27]. The simulated schematic for the Moison model is given in Fig. 11(a) and the Al and Ga concentration profiles are shown in Fig. 11(b). As with the simple linear diffusion model, atomic sites were populated randomly and the results from 10 independent configurations were averaged together. Each interface was simulated separately using a different supercell for each.

Fig. 10 shows that there is a good agreement between experiment and simulation for both types of interface and that the Moison model provides the closest match to the experimental results of all the models considered. For instance, the GaAs-on-AlAs model produces a constant interface width of $\sim 3\text{ML}$ over the entire thickness range. Dumbbells 11-12 are interfacial at small depths but, as the thickness increases, dumbbell 12 becomes GaAs-like and dumbbell 10 slowly becomes interfacial. Thus, the interface position slowly drifts by 1ML from between dumbbells 11-12 to between dumbbells 10-11. In comparison, the interface width of the AlAs-on-GaAs model increases from $\sim 2\text{ML}$ up to $\sim 8\text{ML}$ over the thickness range. At small depths it is unlikely that any Ga atoms are present in the Group III columns of dumbbells 22-27 due to the small percentage of Ga and the interface width is dominated by dumbbells 20-21. However, as the thickness is increased, the number of Ga atoms in dumbbells 22-27 slowly rises and the interface widens accordingly. In contrast, the interface position only shifts by 2ML into the AlAs region due to the asymmetrical concentration profile i.e. the inflection point of the fitted function is kept close to dumbbell 20 due to the large drop in Ga concentration in that dumbbell. The Moison model therefore demonstrates that different diffusion profiles can be identified by HAADF imaging if experiments are conducted over a thickness series.

4. Conclusions

Complex interfacial structures can exhibit a range of characteristics which are difficult to interpret directly from HAADF imaging. For instance, the various models of the AlAs/GaAs system showed that the measured interface width can change with thickness in a complicated manner. Hence, the combination of atomic-resolution HAADF imaging with the simulation of interfacial models is necessary for a deeper and more complete analysis of interfacial structures. Such analysis should be performed over a range of experimental thicknesses using likely candidate models for comparison. In this paper, a series of models were simulated to demonstrate the behaviour of some common types of interfacial structures in the AlAs/GaAs system and the results were compared to experiment.

The perfect model confirmed that an abrupt interface would be characterised as such if analysed by HAADF imaging. In comparison, the vicinal/sawtooth models illustrated that the nature of the stepping and the vicinal angle can produce significant differences in the measured attributes. These models also established that the interface width is dependent on

the type of material that is present in the top part of the specimen. This has implications for the way in which a specimen of a vicinal structure is prepared and how it is positioned in the microscope as this determines which type of material is projected through first of all. In addition, it was also shown that the projection through a low Z material, such as AlAs, allows deep compositional changes to be detected due to the long channelling depths of low Z columns.

Although three of the vicinal/sawtooth interfaces produced behaviour similar to the experimental GaAs-on-AlAs interface, it is unlikely that regular steps are created by the MBE process. The more realistic random step model generated a variation in the interface width that resembled the experimental AlAs-on-GaAs plot. However, a vicinal angle larger than the usual tolerance in MBE is probably required for a better match with experiment. The simple linear diffusion model revealed that the interface width decreases substantially with thickness. In contrast, the non-linear concentration profile of the Moison diffusion model gave the closest agreement with experiment. This model replicated the variation in the interface width observed for both types of interface and is the most likely candidate for the underlying structure of the interfaces.

Acknowledgements

This work was funded by the Engineering and Physical Sciences Research Council under grants GR/S41036/01 and EP/F002610/1 with support for one of the authors (MF) from the Doctoral Training Account. We are grateful to Martin Holland for growing the MBE materials and to Brian Miller for specimen preparation. We would also like to thank Andrew Bleloch, Mhairi Gass, Uwe Falke and Meiken Falke for SuperSTEM technical support and advice.

Figure captions

Fig. 1. Schematic of the perfect AlAs/GaAs supercell viewed down the [110] direction. Inset shows an enlarged view of 2×1 [110]-unit cells with probe positions highlighted for one dumbbell.

Fig. 2. (a) The variation of the column ratio for bulk GaAs and bulk AlAs as a function of specimen thickness for simulation and experiment. (b) Simulated real space intensity as a function of thickness for Al, Ga and As (from GaAs) columns. Intensity was integrated over a radius of 0.2\AA around each column.

Fig. 3. Side view schematic of the perfect model. The simulated interface position is overlaid.

Fig. 4. The variation of interface width as a function of specimen thickness for the perfect, 108nm repeat length ($R=108\text{nm}$) sawtooth and 19.2nm repeat length ($R=19.2\text{nm}$) sawtooth simulated models. For each sawtooth model, GaAs-projection and AlAs-projection cases are provided. Also shown are the experimental data points for the AlAs-on-GaAs and GaAs-on-AlAs interfaces.

Fig. 5. Side view schematic of the 108nm repeat length sawtooth model. The step length is 7.2nm. The simulated interface position is overlaid for the GaAs-projection and AlAs-projection interfaces.

Fig. 6. Side view schematic of the 19.2nm repeat length sawtooth model. The step length is 1.2nm. The simulated interface position is overlaid for the GaAs-projection and AlAs-projection interfaces.

Fig. 7. Simulated HAADF column signal (i.e. minus background) as a function of thickness for the Group III column of dumbbell 7 in the 19.2nm repeat length sawtooth model. The position of the GaAs steps are overlaid. Also shown are the equivalent column signals for bulk Ga (from GaAs) and bulk Al (from AlAs) columns.

Fig. 8. (a) Side view schematic of the random step 0.6° interface model. The simulated interface position is overlaid for the AlAs-projection case. (b) The variation of interface width as a function of specimen thickness for the random step interface model with vicinal angles of 0.2° , 0.3° and 0.6° . Also shown are the experimental data points for the AlAs-on-GaAs and GaAs-on-AlAs interfaces.

Fig. 9. (a) Side view schematic of the simple linear diffusion model. The simulated interface position is overlaid. (b) The change in concentration of Al and Ga across the simple linear diffusion model.

Fig. 10. The variation of interface width as a function of specimen thickness for the simple linear diffusion and the Moison diffusion models. Also shown are the experimental data points for the AlAs-on-GaAs and GaAs-on-AlAs interfaces.

Fig. 11. (a) Side view schematic of the Moison diffusion model. The simulated interface position is overlaid for the GaAs-on-AlAs and AlAs-on-GaAs interfaces. (b) The change in concentration of Al and Ga across the Moison diffusion model.

Reference

- [1] J. H. Davies, *The physics of low-dimensional semiconductors*, Cambridge University Press (2005)
- [2] S. M. Sze, *Semiconductor devices: physics and technology*, John Wiley & Sons, INC. (2002)
- [3] L. Clement, C. Borowiak, R. Galand, K. Lepinay, F. Lorut, R. Pantel, G. Servanton, R. Thomas, P. Vannier and N. Bicaïs, *Journal of Physics: Conference Series* 326 (2011) 012008
- [4] K. Y. Cheng, *Proceedings of the IEEE* Vol. 85 (1997) No. 11
- [5] M. Valera, A. R. Lupini, K. van Benthem, A. Y. Borisevich, M. F. Chisholm, N. Shibata, E. Abe, S. J. Pennycook, *Annual Review of Materials Research* Vol. 35 (2005) 359-569
- [6] T. Noda, N. Sumida, S. Koshiba, S. Nishioka, Y. Negi, E. Okunishi, Y. Akiyama, H. Sakaki, *Journal of Crystal Growth* 278 (2005) 569–574
- [7] N. Tanaka, *Science and Technology of Advanced Materials* 9 (2008) 014111
- [8] K. van Benthem and S. J. Pennycook, *Applied Physics A: Materials Science & Processing*

Vol. 96 (2009) 161-169

[9] S. J. Pennycook, D. E. Jesson, *Physical Review Letters* 64 (1990) 938-941

[10] S. J. Pennycook, D. E. Jesson, *Ultramicroscopy* 37 (1991) 14-38

[11] S. J. Pennycook, B. Rafferty, P. D. Nellist, *Microscopy Microanalysis* 6 (2000) 343-352

[12] D. O. Klenov, S. Stemmer, *Ultramicroscopy* 106 (2006) 889-901

[13] S. I. Molina, M. P. Guerrero, P. L. Galindo, D. L. Sales, M. Varela and S. J. Pennycook, *Journal of Electron Microscopy* 60 (2011) 29–33

[14] S. Van Aert, P. Geuens, D. van Dyck, C. Kisielowski, J. R. Jinschek, *Ultramicroscopy* 107 (2007) 551-558

[15] P. D. Robb and A. J. Craven, *Ultramicroscopy* 109 (2008) 61-69

[16] P. D. Robb, M. Finnie, P. Longo and A. J. Craven, *Ultramicroscopy* 114 (2012) 11-19

[17] D. A. Muller, B. Edwards, E. J. Kirkland, J. Silcox, *Ultramicroscopy* 86 (2001) 371–380

[18] K. Ishizuka, *Ultramicroscopy* 90 (2002) 71–83

[19] C. Dwyer, J. Etheridge, *Ultramicroscopy* 96 (2003) 343-360

[20] D. A. Blom, *Ultramicroscopy* 112 (2012) 69–75

[21] J. M. LeBeau and S. Stemmer, *Ultramicroscopy* 108 (2008) 1653–1658

[22] J. M. LeBeau, S. D. Findlay, L. J. Allen and S. Stemmer, *Physical Review Letters* 100 (2008) 206101

- [23] J. M. LeBeau, S. D. Findlay, X. Wang, A. J. Jacobson, L. J. Allen, S. Stemmer, *Physical Review B* 79 (2009)
- [24] A. Rosenauer, K. Gries, K. Muller, A. Pretorius, M. Showalter, A. Avramescu, K. Engl, S. Lutgen, *Ultramicroscopy* 109 (2009) 1171–1182.
- [25] N. Ikarashi and K. Ishida, *Journal of Materials Science: Materials in Electronics* 7 (1996) 285-295
- [26] N. Ikarashi, T. Baba, K. Lshida, *Applied Physics Letters* 62 (1993) 1632-1634
- [27] J. M. Moison, C. Guille, F. Houzay, F. Barthe, M. Van Rompay, *Physical Review B* Volume 40 9 (1989) 6149-6162
- [28] N. Dellby, O L. Krivanek, P. D. Nellist, P. E. Batson, A. R. Lupini, *Journal of Microscopy* 50(3) (2001) 177-185
- [29] O. L. Krivanek, N. Dellby, A. R. Lupini, *Ultramicroscopy* 78 (1999) 1-11
- [30] R. F. Egerton, *Electron energy-loss spectroscopy in the electron microscope*, 2nd edition, Plenum Press (1996)
- [31] C. P. Scott, A. J. Craven, P. Hatto, C. Davies, *Journal of Microscopy* Vol. 182 (1996) 186-191
- [32] E. J. Kirkland, *Advanced Computing in Electron Microscopy*, Plenum Press, New York (1998)
- [33] J. S. Reid, Debye-Waller factors of zinc-blende structure materials-a lattice dynamical comparison, *Acta Crystallographica Section A, Foundations of Crystallography* A39 1-13 (1983)
- [34] <www.scotgrid.ac.uk>, (2012)
- [35] C. Dwyer, *Ultramicroscopy* 110 (2010) 195–198

Figures

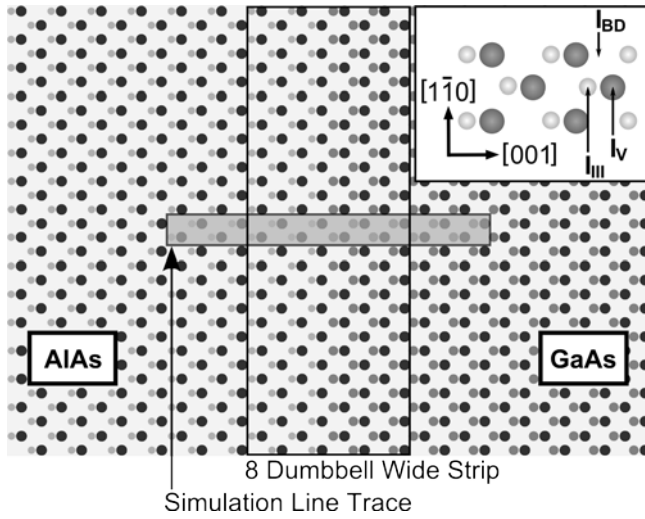


Fig. 1. Schematic of the perfect AlAs/GaAs supercell viewed along the $[110]$ direction. Inset shows an enlarged view of 2×1 $[110]$ -unit cells with probe positions highlighted for one dumbbell.

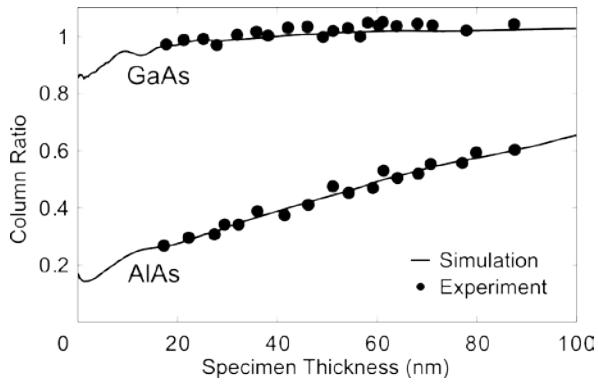


Fig. 2. (a) The variation of the column ratio for bulk GaAs and bulk AlAs as a function of specimen thickness for simulation and experiment.

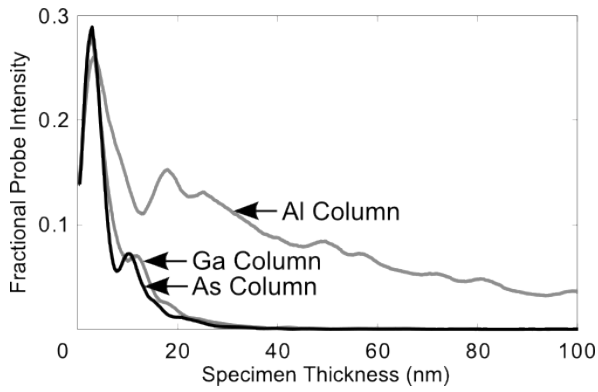


Fig. 2. (b) Simulated real space intensity as a function of thickness for Al, Ga and As (from GaAs) columns. Intensity was integrated over a radius of 0.2\AA around each column.

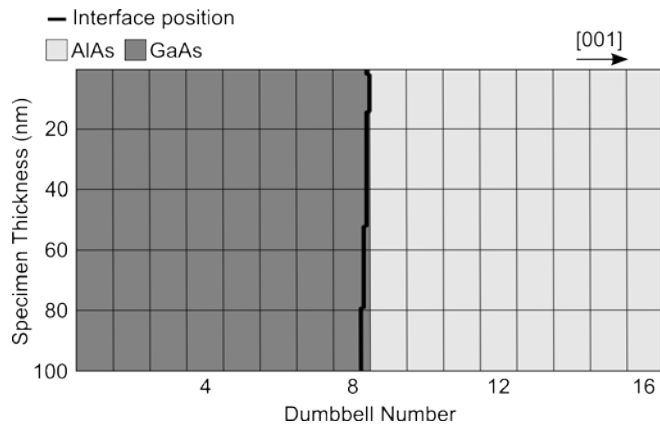


Fig. 3. Side view schematic of the perfect model. The simulated interface position is overlaid.

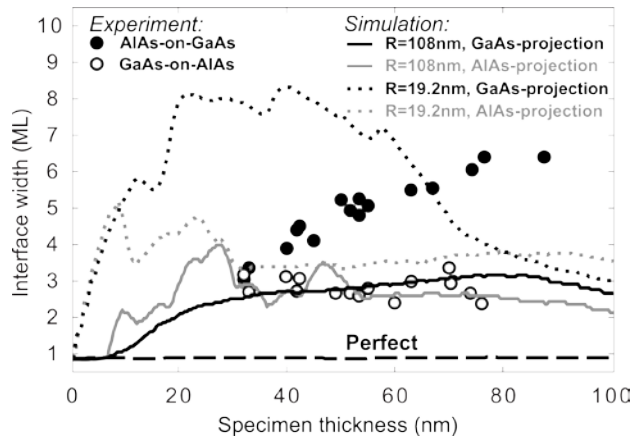


Fig. 4. The variation of interface width as a function of specimen thickness for the perfect, 108nm repeat length (R=108nm) sawtooth and 19.2nm repeat length (R=19.2nm) sawtooth simulated models. For each sawtooth model, GaAs-projection and AlAs-projection cases are provided. Also shown are the experimental data points for the AlAs-on-GaAs and GaAs-on-AlAs interfaces.

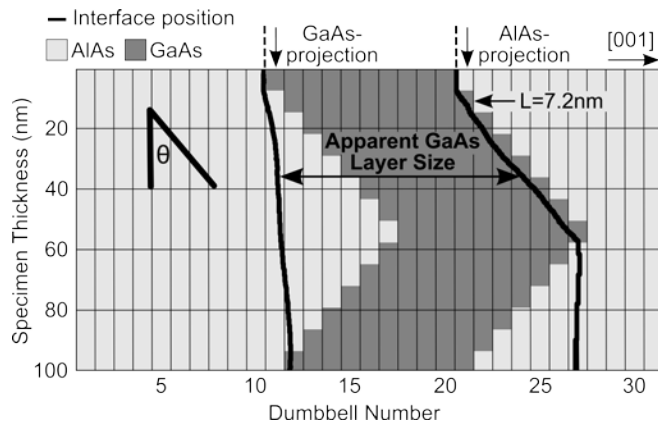


Fig. 5. Side view schematic of the 108nm repeat length sawtooth model. The step length is 7.2nm. The simulated interface position is overlaid for the GaAs-projection and AlAs-projection interfaces.

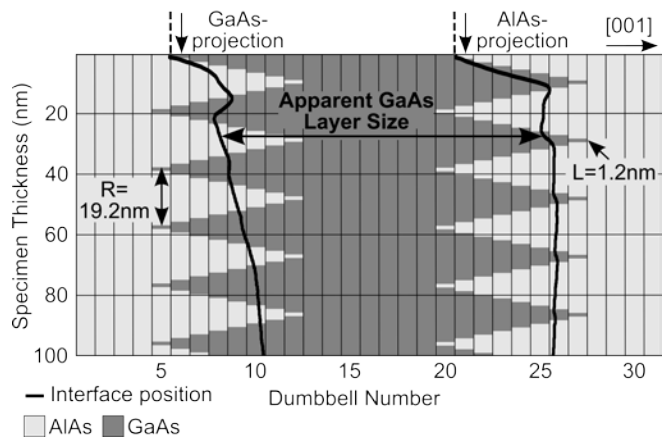


Fig. 6. Side view schematic of the 19.2nm repeat length sawtooth model. The step length is 1.2nm. The simulated interface position is overlaid for the GaAs-projection and AlAs-projection interfaces.

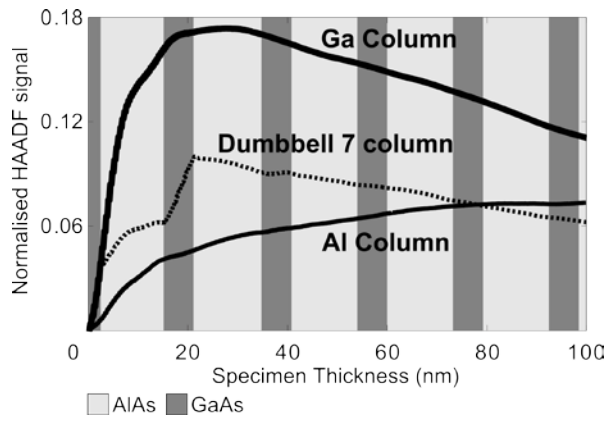


Fig. 7. Simulated HAADF column signal (i.e. minus background) as a function of thickness for the Group III column of dumbbell 7 in the 19.2nm repeat length sawtooth model. The position of the GaAs steps are overlaid. Also shown are the equivalent column signals for pure Ga (from GaAs) and pure Al (from AlAs) columns.

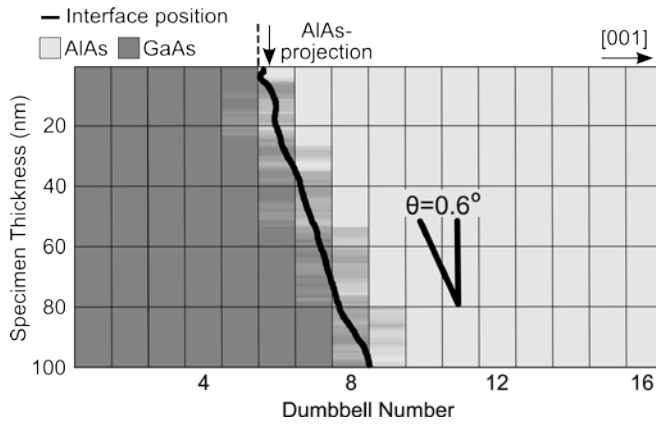


Fig. 8(a). Side view schematic of the random step 0.6° interface model. The simulated interface position is overlaid for the AlAs-projection case.

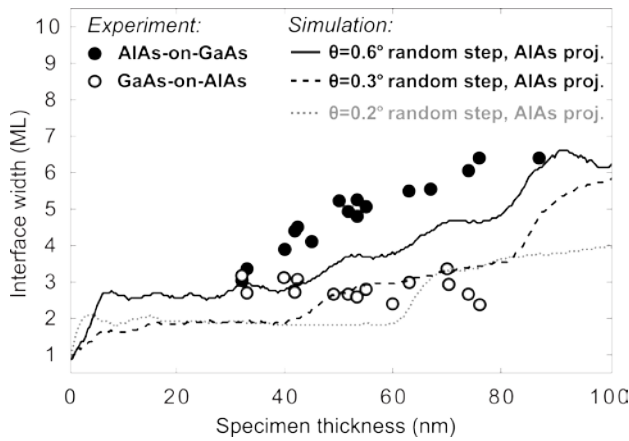


Fig. 8(b). The variation of interface width as a function of specimen thickness for the random step interface model with vicinal angles of 0.2° , 0.3° and 0.6° . Also shown are the experimental data points for the AlAs-on-GaAs and GaAs-on-AlAs interfaces.

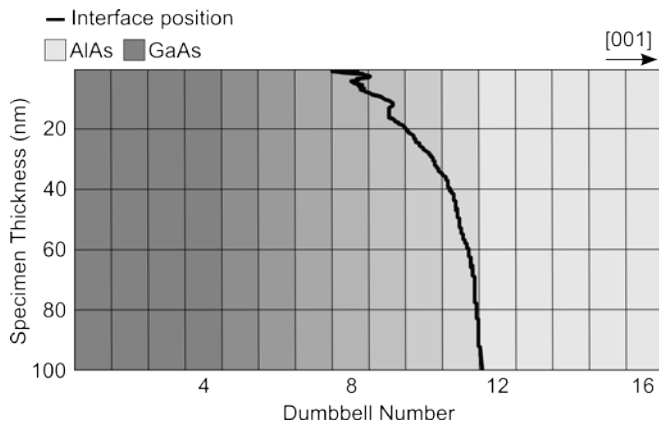


Fig. 9(a). Side view schematic of the simple linear diffusion model. The simulated interface position is overlaid.

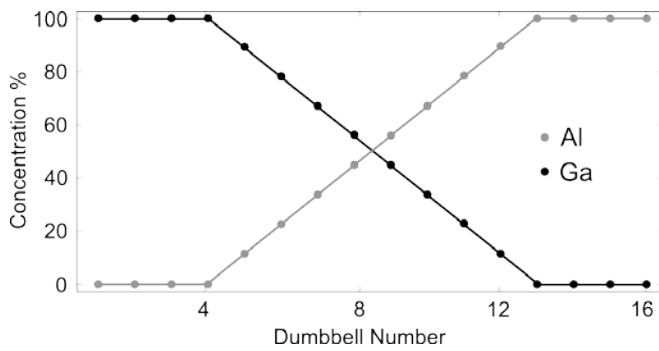


Fig. 9(b). The change in concentration of Al and Ga across the simple linear diffusion model.

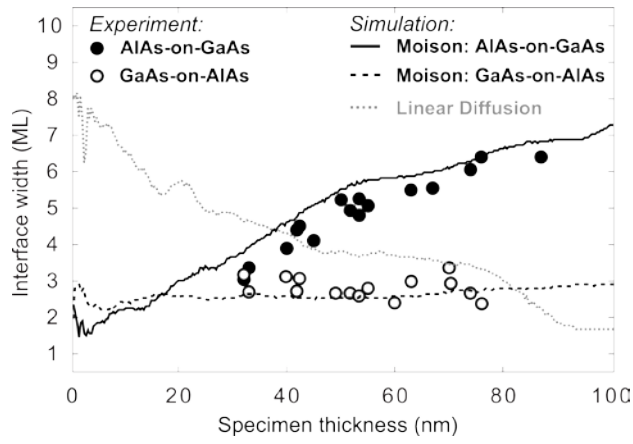


Fig. 10. The variation of interface width as a function of specimen thickness for the simple linear diffusion and the Moison diffusion models. Also shown are the experimental data points for the AlAs-on-GaAs and GaAs-on-AlAs interfaces.

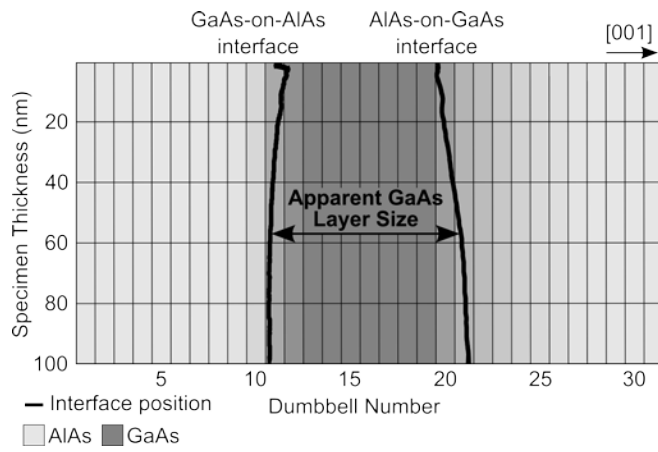


Fig. 11(a). Side view schematic of the Moison diffusion model. The simulated interface position is overlaid for the GaAs-on-AlAs and AlAs-on-GaAs interfaces.

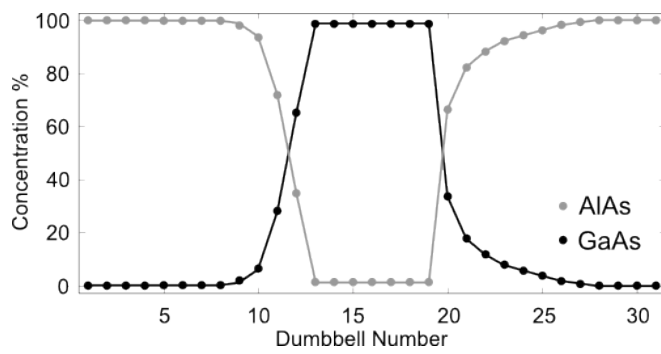


Fig. 11(b). The change in concentration of Al and Ga across the Moison diffusion model.

Reference

- [1] J. H. Davies, The physics of low-dimensional semiconductors, Cambridge University Press (2005)
- [2] S. M. Sze, Semiconductor devices: physics and technology, John Wiley & Sons, INC. (2002)
- [3] L. Clement, C. Borowiak, R. Galand, K. Lepinay, F. Lorut, R. Pantel, G. Servanton, R. Thomas, P. Vannier and N. Bicaïs, Journal of Physics: Conference Series 326 (2011) 012008
- [4] K. Y. Cheng, Proceedings of the IEEE Vol. 85 (1997) No. 11
- [5] M. Valera, A. R. Lupini, K. van Benthem, A. Y. Borisevich, M. F. Chisholm, N. Shibata, E. Abe, S. J. Pennycook, Annual Review of Materials Research Vol. 35 (2005) 359-569
- [6] T. Noda, N. Sumida, S. Koshiba, S. Nishioka, Y. Negi, E. Okunishi, Y. Akiyama, H. Sakaki, Journal of Crystal Growth 278 (2005) 569–574
- [7] N. Tanaka, Science and Technology of Advanced Materials 9 (2008) 014111
- [8] K. van Benthem and S. J. Pennycook, Applied Physics A: Materials Science & Processing Vol. 96 (2009) 161-169
- [9] S. J. Pennycook, D. E. Jesson, Physical Review Letters 64 (1990) 938-941
- [10] S. J. Pennycook, D. E. Jesson, Ultramicroscopy 37 (1991) 14-38
- [11] S. J. Pennycook, B. Rafferty, P. D. Nellist, Microscopy Microanalysis 6 (2000) 343-352
- [12] D. O. Klenov, S. Stemmer, Ultramicroscopy 106 (2006) 889-901
- [13] S. I. Molina, M. P. Guerrero, P. L. Galindo, D. L. Sales, M. Varela and S. J. Pennycook, Journal of Electron Microscopy 60 (2011) 29–33

- [14] S. Van Aert, P. Geuens, D. van Dyck, C. Kisielowski, J. R. Jinschek, *Ultramicroscopy* 107 (2007) 551-558
- [15] P. D. Robb and A. J. Craven, *Ultramicroscopy* 109 (2008) 61-69
- [16] P. D. Robb, M. Finnie, P. Longo and A. J. Craven, *Ultramicroscopy* 114 (2012) 11-19
- [17] D. A. Muller, B. Edwards, E. J. Kirkland, J. Silcox, *Ultramicroscopy* 86 (2001) 371–380
- [18] K. Ishizuka, *Ultramicroscopy* 90 (2002) 71–83
- [19] C. Dwyer, J. Etheridge, *Ultramicroscopy* 96 (2003) 343-360
- [20] D. A. Blom, *Ultramicroscopy* 112 (2012) 69–75
- [21] J. M. LeBeau and S. Stemmer, *Ultramicroscopy* 108 (2008) 1653–1658
- [22] J. M. LeBeau, S. D. Findlay, L. J. Allen and S. Stemmer, *Physical Review Letters* 100 (2008) 206101
- [23] J. M. LeBeau, S. D. Findlay, X. Wang, A. J. Jacobson, L. J. Allen, S. Stemmer, *Physical Review B* 79 (2009)
- [24] A. Rosenauer, K. Gries, K. Muller, A. Pretorius, M. Showalter, A. Avramescu, K. Engl, S. Lutgen, *Ultramicroscopy* 109 (2009) 1171–1182.
- [25] N. Ikarashi and K. Ishida, *Journal of Materials Science: Materials in Electronics* 7 (1996) 285-295
- [26] N. Ikarashi, T. Baba, K. Lshida, *Applied Physics Letters* 62 (1993) 1632-1634
- [27] J. M. Moison, C. Guille, F. Houzay, F. Barthe, M. Van Rompay, *Physical Review B* Volume 40 9 (1989) 6149-6162

- [28] N. Dellby, O L. Krivanek, P. D. Nellist, P. E. Batson, A. R. Lupini, *Journal of Microscopy* 50(3) (2001) 177-185
- [29] O. L. Krivanek, N. Dellby, A. R. Lupini, *Ultramicroscopy* 78 (1999) 1-11
- [30] R. F. Egerton, *Electron energy-loss spectroscopy in the electron microscope*, 2nd edition, Plenum Press (1996)
- [31] C. P. Scott, A. J. Craven, P. Hatto, C. Davies, *Journal of Microscopy* Vol. 182 (1996) 186-191
- [32] E. J. Kirkland, *Advanced Computing in Electron Microscopy*, Plenum Press, New York (1998)
- [33] J. S. Reid, Debye-Waller factors of zinc-blende structure materials-a lattice dynamical comparison, *Acta Crystallographica Section A, Foundations of Crystallography* A39 1-13 (1983)
- [34] C. Dwyer, *Ultramicroscopy* 110 (2010) 195–198